Nucleic Acids Research, 2024, 1–12
https://doi.org/10.1093/nar/gkae377
RNA and RNA-protein complexes

Structure-based characterization and compound identification of the wild-type THF class-II riboswitch

Chunyan Li[1,†], Xiaochen Xu[2,†], Zhi Geng[3,†], Luqian Zheng[4], Qianqian Song[1], Xin Shen[1], Jingjing Wu[5], Jin zhao[5], Hongcheng Li[1], Mengqi He[1], Xiaoqing Tai[1], Long Zhang[1], Jinbiao Ma[5], Yuhui Dong[3,6] and Aiming Ren[1,*]

[1]Life Sciences Institute, Second Affiliated Hospital of Zhejiang University School of Medicine, Zhejiang Key Laboratory of Biotherapy, Zhejiang University, Hangzhou 310058, China
[2]The Eighth Affiliated Hospital, Sun Yat-sen University, Shenzhen 518033, China
[3]Beijing Synchrotron Radiation Facility, Institute of High Energy Physics, Chinese Academy of Sciences, Beijing 100049, China
[4]College of Life Sciences, Anhui Normal University, Wuhu 241000 Anhui, China
[5]State Key Laboratory of Genetic Engineering, Collaborative Innovation Center of Genetics and Development, Department of Biochemistry and Biophysics, School of Life Sciences, Fudan University, Shanghai 200438, China
[6]University of Chinese Academy of Sciences, Beijing 100049, China

[*]To whom correspondence should be addressed. Tel: +86 571 88981228; Fax: +86 571 88981336; Email: aimingren@zju.edu.cn
[†]The first three authors should be regarded as Joint First Authors.

Abstract

Riboswitches are conserved regulatory RNA elements participating in various metabolic pathways. Recently, a novel RNA motif known as the *folE* RNA motif was discovered upstream of *folE* genes. It specifically senses tetrahydrofolate (THF) and is therefore termed THF-II riboswitch. To unravel the ligand recognition mechanism of this newly discovered riboswitch and decipher the underlying principles governing its tertiary folding, we determined both the free-form and bound-form THF-II riboswitch in the wild-type sequences. Combining structural information and isothermal titration calorimetry (ITC) binding assays on structure-based mutants, we successfully elucidated the significant long-range interactions governing the function of THF-II riboswitch and identified additional compounds, including alternative natural metabolites and potential lead compounds for drug discovery, that interact with THF-II riboswitch. Our structural research on the ligand recognition mechanism of the THF-II riboswitch not only paves the way for identification of compounds targeting riboswitches, but also facilitates the exploration of THF analogs in diverse biological contexts or for therapeutic applications.

Graphical abstract

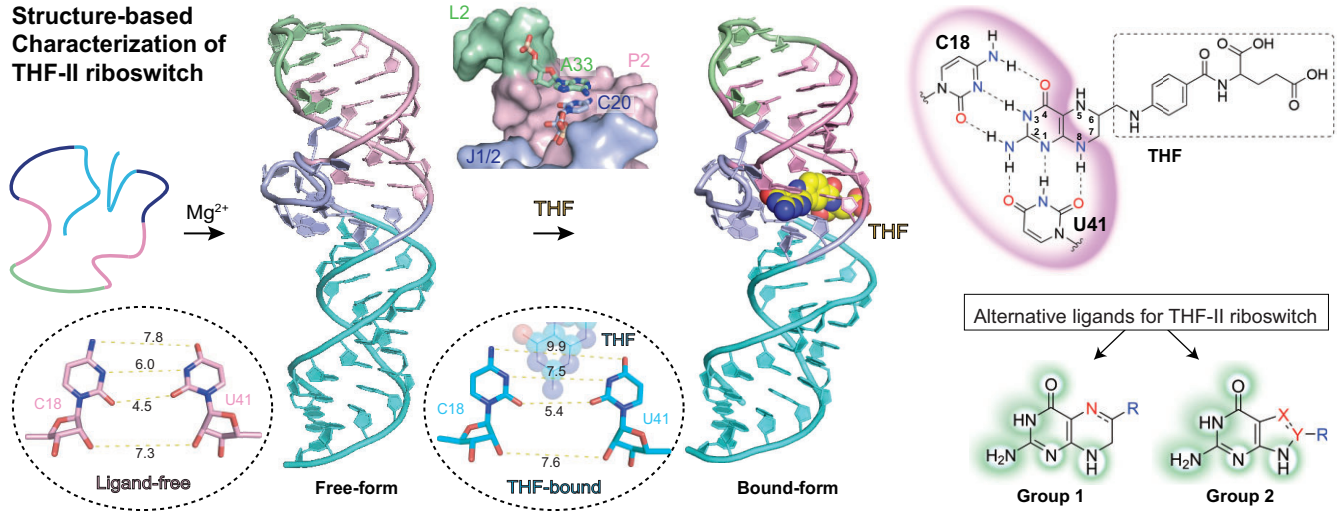

Received: March 14, 2024. **Revised:** April 23, 2024. **Editorial Decision:** April 24, 2024. **Accepted:** April 26, 2024

Introduction

Riboswitches are conserved regulatory elements embedded in non-coding RNA region. They consist of a highly conserved sensing domain and an adjacent variable expression platform (1–4). The sensing domain selectively recognizes distinct metabolites, inducing a global conformational shift of the riboswitch. This, in turn, impacts the expression platform and governs downstream gene expression (5–8). Unraveling the mechanism of action of these structured RNA elements would significantly enrich our comprehension of RNA-based gene regulation and the functional diversity of non-coding RNAs.

Thus far, over 55 classes of riboswitches have been identified (9) with the largest group consists of riboswitches sensing coenzymes and their derivatives (9,10). These coenzymes and derivatives play critical roles in cellular biocatalysis processes (11,12). Tetrahydrofolate (THF), the coenzyme form of vitamin B9, consists of three distinct parts: tetrahydropterin part, *para*-aminobenzoic acid part and glutamic acid part (Figure 1A and Supplementary Figure S1A). Serving as carriers and donors of chemically active one-carbon units, such as methyl or methylene group, THF and its various natural derivatives are vital in one-carbon metabolism and play indispensable roles across the three kingdoms of life (13,14).

In 2010, the first THF-sensing riboswitch motif, known as THF-I riboswitch, was identified, which is often associated with folate uptake transporter *folT* genes or certain folate biosynthesis genes *folE*, *folC* and *folQPBK* in Gram-positive bacteria, such as *Clostridiales* and *Lactobacillales* (15). The consensus secondary structure of the THF-I riboswitch comprises four stems and an additional pseudoknot, with an internal bubble connecting stem P1 and P2, as well as a three-way junction bulge connecting stems P2, P3 and P4. Subsequent structural studies revealed that the THF-I riboswitch specifically recognizes the reduced tetrahydropterin part of THF or its derivatives using two well-defined binding pockets (16,17). In 2019, a simpler conserved RNA motif, termed the '*folE* motif,' was discovered as the second THF-sensing riboswitch (THF-II riboswitch), which were predominantly found in the 5′-UTR of the *folE* gene in a limited range of Gram-negative bacteria (18).

Compared to THF-I riboswitches, THF-II riboswitches are shorter in length, featuring a compact secondary structure with two stems connected by one internal bubble. Despite this smaller size, THF-II riboswitches maintain a binding affinity comparable to THF and related derivatives (15,18). Although both THF-I and THF-II riboswitch function as genetic 'OFF' switches at translation level, they employ distinct mechanisms for downstream gene regulation (15,18). In THF-I riboswitches, ligand binding triggers the formation of a downstream hairpin, preventing the interaction between RBS and ribosome. However, the THF-II riboswitches seem to lack the obvious expression platform as their RBS is integrated into the sensing domain. Ligand binding to THF-riboswitches directly accelerates the formation of anti-RBS stem, thereby resisting ribosome binding and hindering translation initiation. These distinct regulatory mechanisms arise from the dissimilarities in their tertiary structures.

To investigate how THF-II riboswitch RNA recognizes the same THF ligand using a distinct RNA fold, and to understand the underlying principles of THF-II riboswitch tertiary folding, we determined the crystal structures of both the free-form and bound-form THF-II riboswitch in wild-type sequences, encompassing the ribosome binding site (RBS). Based on the structural information and isothermal titration calorimetry (ITC) binding assays on structure-based mutants, we identified additional compounds capable of binding to the THF-II riboswitch through structure-guided rational design. Overall, our structural studies on ligand-RNA interactions provide valuable insights into the ligand recognition mechanism, facilitating the design and application of THF analogs across diverse biological contexts.

Materials and methods

RNA preparation

We have selected a large number of wild-type THF-II riboswitch sequences from different species, including *Ochrobactrum*, *Brucella*, *Mesorhizobium* and environment (18). All RNA samples of THF-II riboswitches were prepared through *in vitro* transcription. To ensure sample homogeneity, the DNA sequence corresponding to the THF-II riboswitch RNA followed by the hepatitis delta virus (HDV) ribozyme was produced via solid-phase synthesis and put into pUT7 plasmid containing T7 promoter, and the plasmid was amplified by polymerase chain reaction (PCR) to produce the DNA template for *in vitro* transcription (19). HDV is a self-cleaving ribozyme that exhibits cleavage activity in the presence of divalent cations (20). *In vitro* transcription was carried out using T7 RNA polymerase at 37°C for 4.5 h, in a system of 100 mM HEPES pH 7.9, 60 mM DTT, 100 μM spermidine, 4 mM NTP, 30 mM $MgCl_2$. Purification of these RNA samples was carried out through urea-denatured polyacrylamide gel electrophoresis (urea-PAGE). The RNA sample was then extracted from the target band by soaking in 0.5× Tris–acetate–EDTA (TAE) buffer at 4°C, precipitated with isopropanol, washed twice with 80% ethanol, and subsequently lyophilized. All the solutions used in RNA preparation were prepared with diethyl pyrocarbonate (DEPC)-treated double-distilled water.

Ligands

Tetrahydrofolate, dihydrofolate, 7,8-dihydroneopterin, tetrahydrobiopterin, guanine, 5-methyl THF, folinic acid, folic acid, 6-biopterin, 8-aminoguanine, 8-azaguanine were purchased from Shanghai Yuanye Bio-Technology Co., Ltd. 8-Methyl guanine was purchased from Bide Pharmatech Ltd (Shanghai).

Crystallization

In crystallization, RNA samples were prepared by annealing at 65°C for 5 minutes(min) followed by incubation on ice for at least 30 min in the buffer containing 70 mM HEPES pH 7.8, 70 mM KCl, 5 mM $MgCl_2$ and 1 mM dithiothreitol (DTT). The THF-II riboswitch complex was prepared by incubating RNA with a ligand at a ratio of 1:15, resulting in a final concentration of 0.4 mM RNA sample on ice for another hour before crystallization. Crystallization screening was performed at 16°C by mixing with reservoir solution at an equimolar ratio using sitting drop vapor diffusion method. Crystals of the THF-II riboswitch in the bound form grew under conditions including 0.08 M NaCl, 0.04 M sodium cacodylate trihydrate (pH 7.0), 25–30% v/v 2-methyl-2,4-pentanediol (MPD) and 0.012 M spermine tetrahydrochloride over one week. Crystals

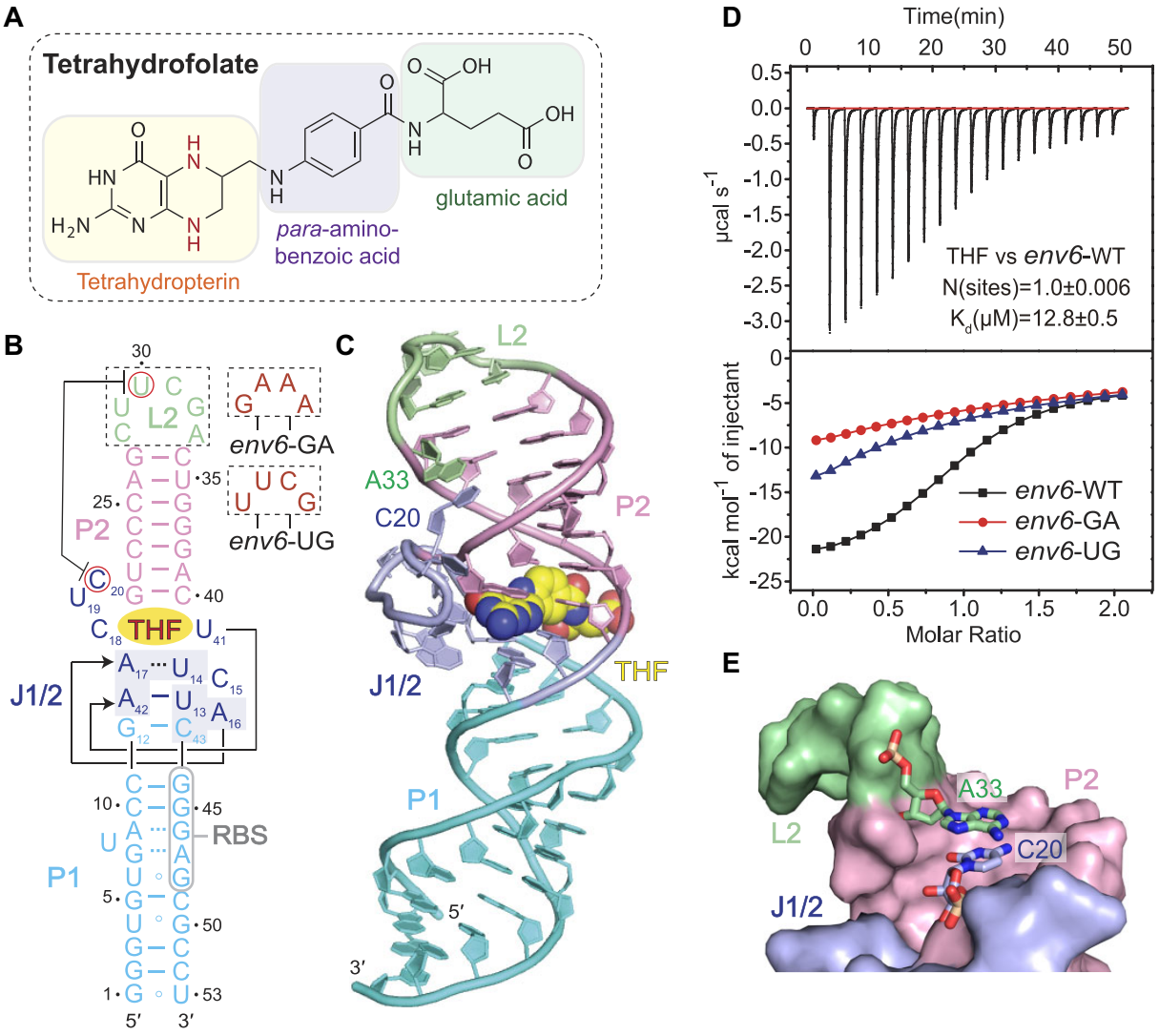

Figure 1. Secondary and tertiary structure of the THF-II riboswitch bound to THF. (**A**) Chemical structure of tetrahydrofolate. (**B**) Schematic representation of the tertiary structure of THF-II riboswitch, same colour code as in the cartoon representation in panel (C) is used. (**C**) Cartoon representation of the tertiary structure of the THF-II riboswitch bound to THF (shown in spheres). (**D**) Isothermal titration calorimetry (ITC) experiment of wild-type (*env6*-WT) THF-II riboswitch and L2 loop mutants (*env6*-GA and *env6*-UG) binding with THF, the corresponding thermodynamic parameters are listed in Supplementary Table S4. (**E**) A33 (shown in sticks) from L2 region forms base stacking interaction with C20 from J1/2 region in the major groove side of stem P2 (shown in surface representation).

of the THF-II riboswitch in the free form were grown under similar conditions to the bound form but with the addition of guanosine triphosphate (GTP). All the crystals were flash-frozen with liquid nitrogen, and X-ray diffraction data were collected at beamline BL19U1 at the Shanghai Synchrotron Radiation Facility (SSRF).

Structure determination

The diffraction data were processed using HKL3000 (HKL Research). The phase problem of *env6* THF-II riboswitch-THF complex was solved with the single-wavelength anomalous diffraction (SAD) method using the diffracted anomalous signal collected from $Ir(NH_3)_6^{3+}$-soaked crystals (21). The structure model was further built in the Coot software suite and refined in Phenix software suite (22–24). All the other structures were solved by the molecular replacement method using the *env6* THF-II riboswitch structure as the initial model with the Phaser program in the CCP4 software suite. The ligand was added into the structure at the last several runs of building and refinement. The statistics of X-ray data and structure refinement are shown in the Supplementary Tables S1–S3.

Isothermal titration calorimetry (ITC)

All ITC experiments were conducted at the National Center for Protein Science Shanghai (NCPSS) using a MicroCal PEAQ-ITC calorimeter at 25 °C. Prior to the titration, the wild-type RNA and mutant RNA samples were dialyzed against ITC buffer (70 mM HEPES pH 7.8, 70 mM KCl, 5 mM $MgCl_2$, 1 mM DTT) overnight at 4°C. Then RNA at a final concentration of 0.1 mM was annealed for 5 min at 65°C, and subsequently cooled on ice for half an hour. The ligand dissolved in ITC buffer and diluted to 1 mM, was titrated into RNA by initial injection of 0.4 μl, followed by

19 serial injections of 2 μl with 150 s intervals between injections and a reference power of 5 μcal s^{-1}. To investigate the impact of $MgCl_2$ on ligand recognition, the wild-type RNA was dialyzed with ITC buffer containing increasing concentrations of $MgCl_2$ (from 0 to 5 mM). The titration data were analyzed using MicroCal PEAQ-ITC Analysis Software, and all the thermodynamic binding parameters are shown in Supplementary Table S4.

Circular dichroism (CD) spectroscopy

CD spectroscopic assays for the *env6* THF-II riboswitch were recorded in a buffer consisting of 10 mM HEPES at pH 7.8 and 10 mM KCl, supplemented with magnesium ions, THF, or both. Background correction was applied using the buffer from each spectrum. In both the absence and presence of 5 mM $MgCl_2$, 12 μM RNA samples were heated to 65°C for 5 min, rapidly cooled on ice for 30 min, and then incubated on ice for 1 h after the addition of THF to achieve a final concentration of 180 μM. CD spectra were measured in a 1 mm cuvette on a Jasco J-1700 spectropolarimeter at 25°C, spanning the wavelength range of 200–350 nm. Thermal melting experiments were conducted at various temperatures using Quartz cuvettes with a 1 mm path length and the ORCD-574 peltier thermostat. Melting curves were recorded at 210 nm with a ramp of 1°C/min and a step size of 0.2, covering a temperature range from 4°C to 95°C. Data analysis was performed using GraphPad Prism 6.0 (25).

Surface plasmon resonance (SPR) measurements

SPR experiments were conducted using a Biacore T200 instrument (GE Healthcare) at 25°C in a buffer comprising 70 mM HEPES at pH 7.8, 70 mM KCl, 5 mM $MgCl_2$ and 0.05% Tween20. The SA Sensor Chip (GE Healthcare) was employed to immobilize 20 μM 5′ biotin-*env6* RNA at a flow rate of 5 μl/min for three cycles, each lasting 5 min. Ligand samples were injected with twofold serial dilutions (ranging from 500 to 7.81 μM of THF, 675 to 5.27 μM of DHF, and 2000 to 8.98 μM of 8-azaguanine) at a flow rate of 30 μl/min during a 120 s association phase. Subsequently, the running buffer was used to dissociate the ligands on the chip for 150 s. The resulting curves were analyzed using the Biacore T200 evaluation software. All curves underwent reference subtraction using the reference channel and blank subtraction using the curves obtained for the buffer cycle. The entire dataset was replicated three times for consistency.

β-Galactosidase report assay

The sequence containing either the WT or mutants of *env6* THF-II riboswitch was cloned into *lacZ* (β-galactosidase) fusion vector pUCm-T (Sangon Biotechnology, Shanghai). *Escherichia coli* DH5α cells carrying these constructs were grown overnight in LB agar plate. Subsequently, the single colony was selected and cultured in LB liquid medium with 100 μg/ml of ampicillin at 37°C for 6–8 h. These cultures were then diluted 1:20 using LB containing the supplements (100 μg/ml ampicillin, 100 μg/ml X-gal). The resulting mixtures were incubated at 37°C for 120 h, and images were recorded.

Results and discussion

According to the reported consensus secondary structure model of *folE* RNA motif, THF-II riboswitch comprises two base-paired stems (P1 and P2) connected by a central large junction (J1/2) (Supplementary Figure S1B, C). Notably, the ribosome binding site (RBS) not only participates in base pairing but also concurrently forms a bulge within the upper part of stem P1. In an effort to preserve the intrinsic folding and function of the THF-II riboswitch while minimizing the potential for unexpected effects arising from mutations, the original wild-type sequence of the riboswitch was preserved from the apical loop of stem P2 to the terminus of stem P1, encompassing the entire RBS (GGGAG) and all the highly conserved nucleotides (label in red) (Supplementary Figure S1B, C).

Overall tertiary fold of *env6* THF-II riboswitch in complex with THF

After screening a large number of *in vitro* transcribed wild-type THF-II riboswitch sequences from different species, high-quality crystals were obtained using a 53 nt RNA sequence of environmental origin, referred to as *env6* THF-II riboswitch in the following description (Figure 1B and Supplementary Figure S1B, C and Supplementary Table S1). ITC experiments demonstrated that the *env6* THF-II riboswitch binds to THF with a binding affinity of $K_d = 12.8 \pm 0.5$ μM, and the stoichiometry of binding approached 1:1. The estimated thermodynamic parameters for the binding were $\Delta H = -21.2 \pm 0.3$ and $\Delta G = -6.7$ kcal mol^{-1} (Figure 1D, Supplementary Figure S2A and Supplementary Table S4).

The overall tertiary architecture of the *env6* THF-II riboswitch in original wild-type sequence is shown in schematic and cartoon representation in Figure 1B, C. Conform to the proposed secondary structure by Breaker's Lab (18), the tertiary fold of THF-II riboswitch contains two stems, P1 (cyan) and P2 (pink), connected by the central junction J1/2 (slate) (Figure 1B, C). The stem P1 (cyan) and the stem P2 (pink) mediated by the junctional region (slate) exhibit co-axial stacking interaction, which further extends to the partially paired apical loop L2, resulting in a rod-like compact helical scaffold for the THF-II riboswitch (Figure 1B, C). The ligand THF is bound in a cavity in the center of THF-II riboswitch, which was formed by the terminus of stem P2 and the asymmetric internal bubble J1/2 (Figure 1B, C). An overview of the base stacking alignment of the *env6* THF-II riboswitch is shown in Supplementary Figure S2B.

Upon inspection of the tertiary structure, two non-canonical G•A base pairs, G7•A47 and A9•G46, are formed in the bulge region of stem P1, mediating continuous stacking between the upper and lower parts of stem P1 (Figure 1B, C and Supplementary Figure S3A–C). Besides, all RBS nucleotides from G44 to G48 are involved in pairing interactions and participate in tertiary stacking (Figure 1B, C). To investigate the role of stem P1, truncation experiments were conducted by replacing stem P1 with a shorter stem containing five Watson-Crick base pairs (termed *env6*-P1D) and no significant effect was observed on the binding affinity of *env6*-P1D with THF ($K_d = 20.0 \pm 2.4$ μM) (Supplementary Figure S3D–F).

In the apical loop L2, one canonical Watson–Crick base pair C28–G32 is formed and stacked on the terminal base pair G27–C34 of stem P2 (Supplementary Figure S4A). A33 is excluded from L2 and protrudes into the major groove side of stem P2, where it forms base stacking interaction with C20 from J1/2 region (Figure 1B, C, E and Supplementary Figure S4A). To detect the potential crosstalk between L2 and J1/2,

we mutated the wild-type L2 sequence with stable GAAA or UUCG tetraloop (Figure 1B and Supplementary Figure S4B). Compared to the wild-type L2 sequence binding to THF with $K_d = 12.8 \pm 0.5$ μM, GAAA or UUCG tetraloop replacement (termed as *env6*-GA and *env6*-UG) dramatically reduces binding affinity and fail to calculate exact binding affinity constants with ITC titration ($K_d \approx 500$ μM and $K_d \approx 200$ μM) (Supplementary Figure S4C-E and Supplementary Table S4). The observation is consistent with the reported in-line probing results that THF addition reduces the spontaneous cleavage of nucleotides residing in the L2 loop and in the junction J1/2 (18).

Typically, RNA molecules with truncated sequence or modified terminal loop are employed for structure determination or function studies. In the case of THF-II riboswitch, we conducted a comparative analysis between the wild-type sequence structure of our *env6* THF-II riboswitch and the previously predicted THF-II riboswitch structure (26), along with the THF-II-lotiTL RNA structure featuring a mutant L2 (PDB: 7W1B) (27). Notably, the cross-talk between L2 and J1/2 was exclusively observed in the *env6* THF-II riboswitch structure (Figure 1E). Mutation of L2 to tetraloops GAAA (*env6*-GA) or UUCG (*env6*-UG) to disrupt the cross-talk between L2 and J1/2 both result in lower THF binding activity in ITC titration (Figure 1D and Supplementary Figure S4, Supplementary Table S4), consistent with the in-line probing results from Breaker's lab (18). Additionally, we conducted β-galactosidase assay to qualitatively assess the impact of the L2-J1/2 cross-talk on the gene regulation behavior of THF-II riboswitch. In this assay, we monitored the production of *lacZ* β-galactosidase in response to THF in *E. coli* DH5α cell by fusing THF-II riboswitch motif (*env6*-WT) and selected mutants (*env6*-GA and *env6*-UG) to a *lacZ* β-galactosidase reporter gene (Supplementary Figure S5A-B). As expected, the expression of *lacZ* β-galactosidase regulated by THF-II riboswitch mutants (*env6*-GA and *env6*-UG) exhibits an elevated expression (Supplementary Figure S5C), contrasting with the repressed expression observed in the wild-type counterpart (*env6*-WT). These observations align with the ITC titration results (Figure 1D) highlight the significance of cross-talk between L2 and J1/2 (Figure 1E), emphasizing the need for caution when making modifications to the RNA sequence during the process of structure determination.

Structural organization of junction J1/2 in *env6* THF-II riboswitch

In the tertiary structure of the *env6* THF-II riboswitch, the central junction J1/2 plays a crucial role in mediating stacking interactions between stems P1 and P2 and contributes to the formation of the THF binding pocket. Most of the residues residing in J1/2 are involved in complex hydrogen-bond networks. A simplified schematic structure diagram highlighting the structural organization of junction J1/2 is shown in Figure 2A. We also present an expended view of J1/2 structural organization in Figure 2B, where the THF ligand is shown as spheres.

Within J1/2, U13 forms a *cis* Watson–Crick base pair with A42 and stacks on the terminal base pair G12–C43 of stem P1. The Watson–Crick edge of U14 forms three hydrogen bonds with the Hoogsteen edge and the non-bridging phosphate oxygen of A17, and stacks on A16 (Figure 2C). C15 protrudes out between U14 and A16, where a sharp turn is formed (Figure 2B). A17•U14 and the stacked A16 interact with the minor groove side of A42–U13 and G12–C43 in a skew orientation (Figure 2C). The Watson–Crick edge of A17 forms two hydrogen bonds with the sugar edge of A42, while the base of A16 forms hydrogen-bonding interactions with the sugar edges of both U13 and C43 (Figure 2D). These complex interactions stabilize the bottom part of J1/2 and provide a structural platform to support the binding of THF. In the upper part of J1/2, C18 and the bound THF form a continuous stacking interaction with the terminal base pair G21–C40 from stem P2 (Figure 2A). The intermediate nucleotides U19 and C20, located between C18 and G21, extend out from the main scaffold (Figure 2B). C20 forms stacking interaction with A33 from L2 on the major groove side of stem P2, potentially contributing to the crosstalk between L2 and J1/2 as discussed above (Figure 1B, C, E and Supplementary Figure S4A).

Next, we conducted ITC titration assays with structure-based mutants, specifically altering the interacting base, to validate the observed complex interaction within the structure. Mutants disrupting the hydrogen-bonding interactions in the U13–A42–A17–U14 quadruple base layer (A42U/C, A17U/C, U14A/G) resulted in loss of THF binding activity (Figure 2E). Within the quadruple base layer U13–A16–C43–G12, C43 forms a canonical Watson–Crick base pair with G12 and two additional hydrogen bonds with A16, further interacting with U13 (Figure 2D). Mutations C43A and C43G had variable effects on THF binding for THF-II riboswitch, with the C43A mutant showing no binding activity to THF, and the C43G mutant exhibiting weak binding (Figure 2F). Mutation of A16 to U or C has a minor effect on the binding capacity of THF-II riboswitch to THF (Figure 2F). U13 is involved in both quadruple base interactions, and mutations to A or G severely affected the binding affinity of THF-II riboswitch to THF (Figure 2F). The retention of some binding activity in the mutants might be due to the maintenance of certain hydrogen bonds or the formation of alternative interactions with surrounding residues (Figure 2F). Overall, our structural analysis and structure-based ITC assays highlight that these two quadruple base interactions U13–A42–A17–U14 (Figure 2C) and U13–A16–C43–G12 (Figure 2D) in junction J1/2 are essential for the binding ability of THF-II riboswitch to THF ligand.

The composition of THF binding pocket in *env6* THF-II riboswitch

As shown in Figure 3A, the tetrahydropterin part of THF (shown in sticks) intercalates into the binding cavity (shown in surface representation) formed between J1/2 and stem P2, while the *para*-amino-benzoic acid part and the glutamic acid part point are positioned outside of the binding cavity without forming any additional interactions with THF-II riboswitch (Figure 3A).

Within the binding cavity, the tetrahydropterin part of THF engages in a base triple interaction with C18 and U41 from J1/2 (Figure 3B-D). Simultaneously, it is sandwiched between the ceiling, formed by G21–C40 from the terminus of stem P2, and the floor, formed by U13–A42–A17–U14 at the junction J1/2 (Figures 2C and 3B–D). The Watson–Crick edge of C18 forms three hydrogen bonds with 2-NH_2, N3, O4 of THF and the Watson–Crick edge of U41 forms three hydrogen bonds with the N1, 2-NH_2, N8 of THF, clamping the tetrahydropterin part of THF within the binding cavity. Notably, a

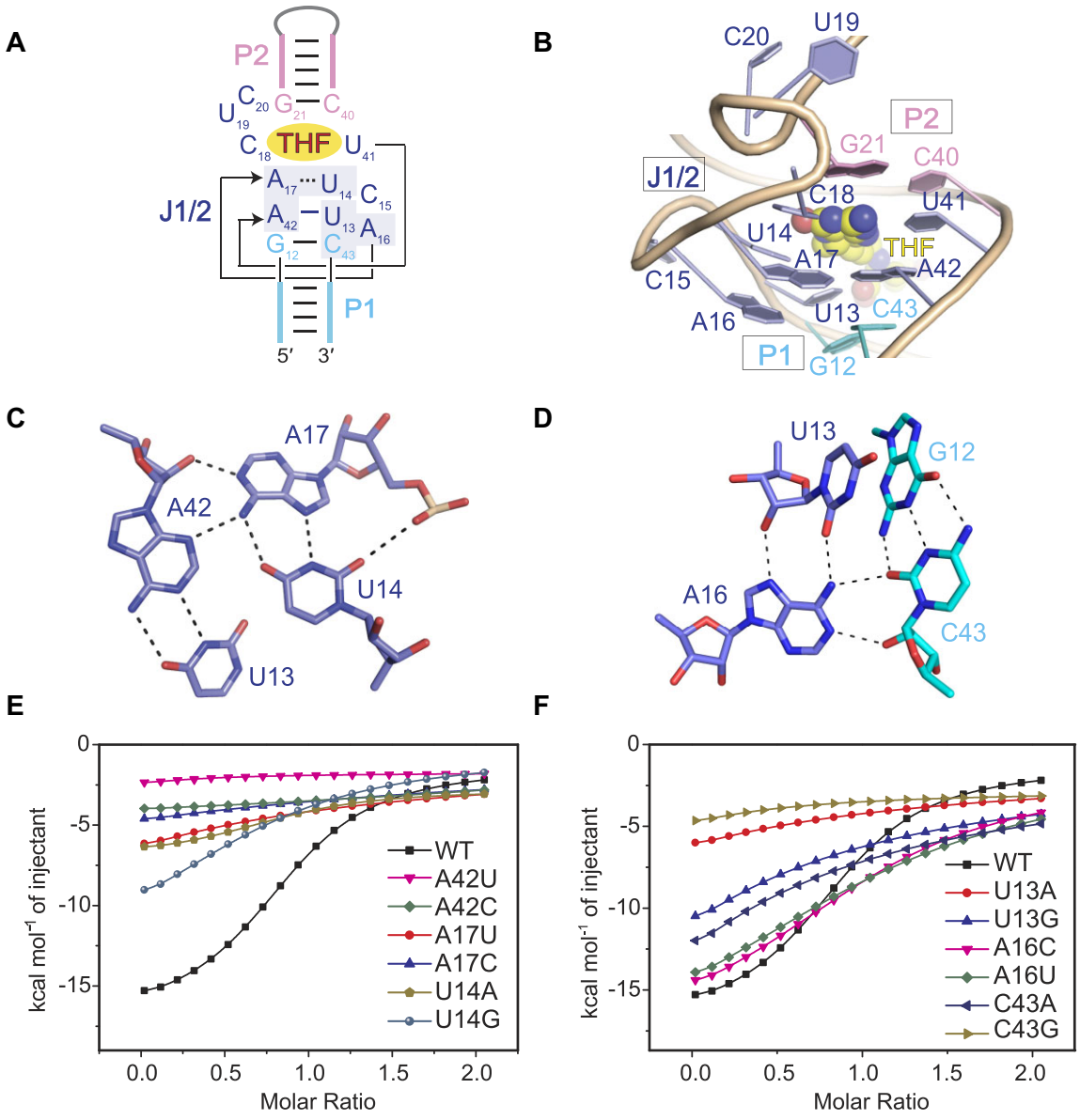

Figure 2. Structural organization of Junction J1/2 in *env6* THF-II riboswitch. (**A**) Schematic secondary structure of THF-II riboswitch highlights the core region. (**B**) Structural organization of junction J1/2 and close-up view of the interactions between junction J1/2 and stem P1. (**C**) Close-up view of the base quadruple U13–U14–A17–A42. The Watson–Crick edge of U14 forms three hydrogen bonds with the Hoogsteen edge of A17. A17•U14 interact with the minor groove side of A42-U13. (**D**) Close-up view of the base quadruple G12–U13–A16–C43. The base of A16 forms two hydrogen bonds with the sugar edges of both U13 and C43. (**E**) Overlay of ITC titration heat plot of wildtype (WT) THF-II riboswitch in comparison with mutants concerning nucleotides in quadruple U13–U14–A17–A42. (**F**) Overlay of ITC titration heat plot of wildtype (WT) THF-II riboswitch in comparison with mutants concerning nucleotides in quadruple G12–U13–A16–C43.

well-defined $2F_{observe} - F_{calculate}$ ($2F_o$–F_c) composite omit electron density map has been calculated for the tetrahydropterin part (contoured at 1.0 σ level), while no reasonable electron density map can be calculated for the *para*-amino-benzoic acid part or the glutamic acid part of THF (Figure 3C). This is consistent with the observation that no significant interaction is formed between the *para*-amino-benzoic acid part and the glutamic acid part of THF with THF-II riboswitch in the tertiary structure (Figure 3A–C).

To verify the observed interactions between THF and THF-II riboswitch in the tertiary structure, mutational analysis combined with ITC experiments was conducted to evaluate the impact of related residues involved in THF recognition. Mutations of C18 or U41 to impair the base triple interactions for the THF ligand (C18A, C18G, U41A and U41G) resulted in a complete loss of binding ability to THF (Figure 3D). Furthermore, we employed β-galactosidase assay to qualitatively assess the impact of critical base mutation on the gene expression regulation behavior of THF-II riboswitch. We fused THF-II riboswitch and mutants (U8C, C18G, U41G and A42U) with *lacZ* β-galactosidase reporter gene (Supplementary Figure S5A, B). Repression of expression was observed in the wild-type (*env6*-WT) THF-II-*lacZ* fusion and the control mutant U8C (U8 does not participate in significant interaction within THF-II riboswitch), whereas expression was enhanced in mutants (C18G, U41G and A42U)

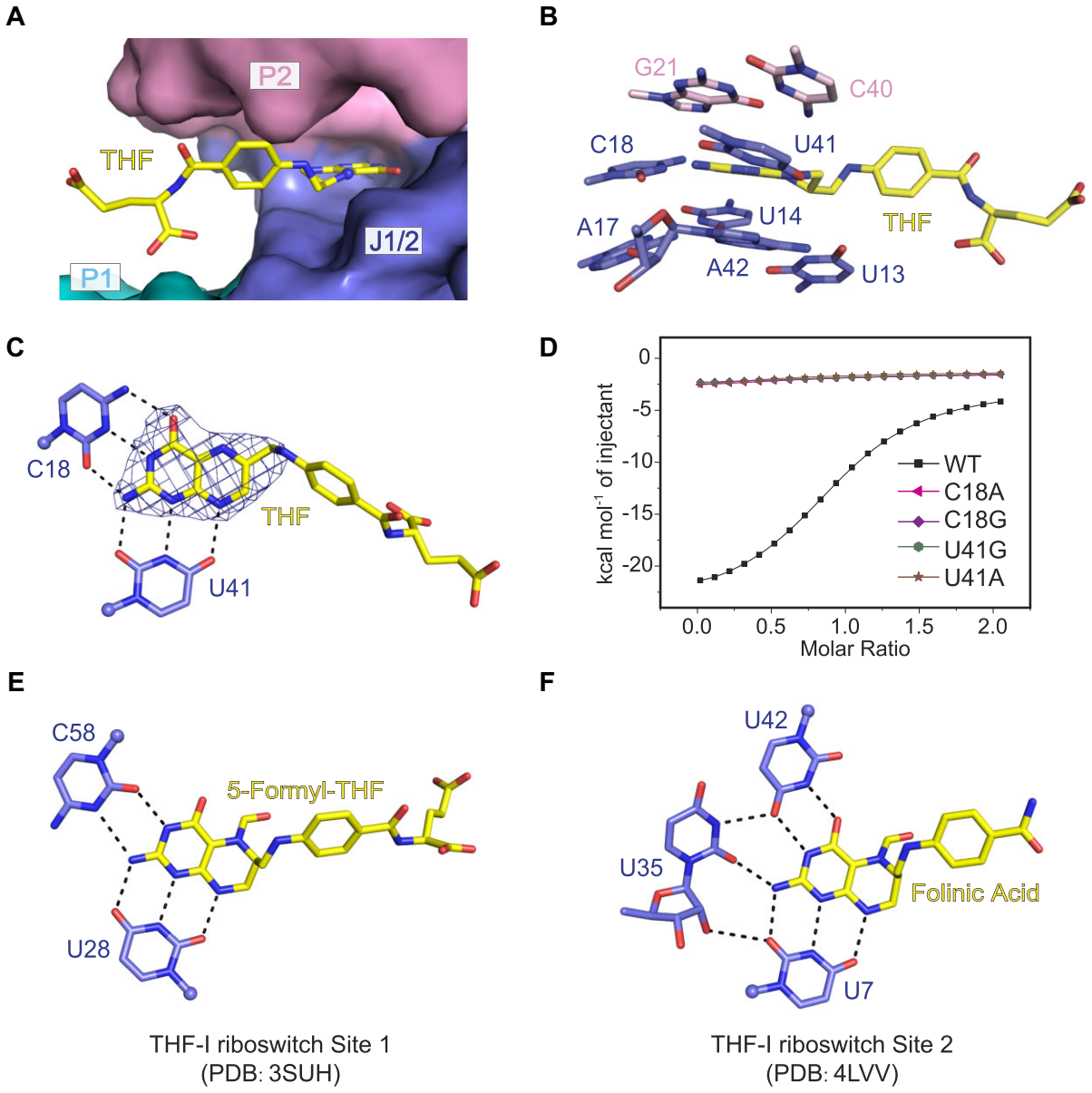

Figure 3. Ligand interaction between THF and the *env6* THF-II riboswitch. (**A**) Surface representation of the THF-II riboswitch binding pocket binding with THF (shown in sticks). The tetrahydropterin part of THF intercalates into the binding cavity formed between J1/2 and stem P2, while the para-amino-benzoic acid part and the glutamic acid part are positioned outside of the binding cavity. (**B**) Tetrahydropterin part of THF participates in the formation of a triple with C18 and U41, which is further stacked between two base platform, G21–C40 and U13–U14–A17–A42. (**C**) Tetrahydropterin part of THF forms extensive hydrogen bond interaction with C18 and U41. The composite omit maps (contoured at 1.0 σ level) of the THF is shown. (**D**) Overlay of ITC titration heat plot of WT THF-II riboswitch in comparison with mutants concerning nucleotides C18 and U41. (**E**) Ligand interaction between the THF-I riboswitch binding pocket 1 with 5-formyl-THF (folinic acid). Tetrahydropterin part of 5-formyl-THF forms hydrogen bond interaction with C58 and U28 (PDB code: 3SUH). (**F**) Ligand interaction between the THF-I riboswitch binding pocket 2 with folinic acid. Tetrahydropterin part of folinic acid forms extensive hydrogen bond interaction with U7, U35 and U42 (PDB code: 4LVV).

(Supplementary Figure S5C). These results confirm the recognition pattern of THF-II riboswitch binding to the THF ligand, as depicted in the three-dimensional structural model.

THF-I riboswitches adopt a tertiary fold characterized by two ligand-binding pockets (Supplementary Figure S6). The first pocket is situated in the minor groove of P3, close to the three-way junction (Supplementary Figure S6A). In this pocket, the folinic acid (5-formyl-THF) ligand (Supplementary Figure S6B) is stabilized by forming three hydrogen bonds with the Watson–Crick edge of U28 and two hydrogen bonds with the Watson–Crick edge of C58 (PDB: 3SUH) (17) (Figure 3E and Supplementary Figure S6C, D). The second binding pocket is positioned at the minor-groove face, nestled between L3 and J2/1 (Supplementary Figure S6A, D). Within this pocket, the folinic acid ligand forms specific hydrogen bonds with certain RNA bases: three with U7, two with U42, and one with O2 of U35 (PDB: 4LVV) (Figure 3F and Supplementary Figure S6D). Notably, U35 establishes two additional hydrogen bonds with U42 and U7, leading to the formation of a base quadruple with the bound ligand.

In contrast to THF-I riboswitch, THF-II riboswitches display a more compact and intricate overall structure. Within

THF-II riboswitches, the ligand is deeply embedded in the binding cavity between J1/2 and P2, creating a confined space around the tetrahydropterin part (Figure 3A). Conversely, THF-I riboswitches feature a more open space around both binding pockets. This distinction in spatial arrangement and confinement contributes to the enhanced selectivity of THF-II riboswitches for THF ligand compared to THF-I riboswitches. THF-I riboswitches can accommodate substantial group modification at position 5 of THF, such as folinic acid (5-methyl THF), whereas THF-II riboswitches cannot.

It is worth noting that while both THF-II riboswitch and the first binding pocket of THF-I riboswitch interact with the tetrahydropterin part of THF using similar residues (C18 and U41 for THF-II riboswitch, and C58 and U28 for the first pocket of THF-I riboswitch) to form base triple interactions, the orientation of the interacting residues C and U is reversed (Figure 3C, E). This reversal in orientation of interacting residues (C and U) in the base triple interactions involving the tetrahydropterin part introduces an extra layer of complexity to the ligand recognition process. This subtle yet significant difference underscores the finely tuned nature of RNA–ligand interactions and highlights the structural diversity achieved within the riboswitch family.

Tertiary structure of free-form THF-II riboswitch

We successfully obtained high diffraction-quality crystals of the ligand-free *env6* THF-II riboswitch from a similar crystallization condition with GTP as additive. To detect the interaction between GTP and *env6* THF-II riboswitch, we perform ITC titration of *env6* THF-II riboswitch and GTP. As shown in Supplementary Figure S7A, *env6* THF-II riboswitch exhibits no binding ability with GTP.

Similar to the THF-bound structure, the ligand-free structure also adopts the rod-like conformation, with stem P1 stacking co-axially with stem P2, mediated by the junctional region J1/2 (Figure 4A and Supplementary Figure S7B). Supplementary Figure S7C highlights the alignment of base stacking between the THF-bound THF-II riboswitch and its ligand-free form. The nucleotides in junctional region J1/2, surrounding the binding pocket adopt similar conformation between the ligand-free structure and THF-bound structure (Supplementary Figure S7D, E). In the bulge region of stem P1, G46–A47–G48 located in the RBS region, participate in the formation of three successive non-canonical base pairs (U6–G48, G7–A47 and A9–G46) (Supplementary Figure S7F). The crosstalk between the loop of stem P2 and the junctional region J1 was also observed, where A33 is excluded from L2 loop and interacts with C20 to form a base stacking (Supplementary Figure S7G). Additionally, the ligand-free structures also exhibit intricate multiple-nucleotide interactions, such as U13–A42–A17–U14 and G12–C43–A16–U13 interactions, situated at the junctional region J1/2 and the top part of stem P2 (Figure 4A and Supplementary Figure S7H, I).

Within the binding pocket of the ligand-free form THF-II riboswitch structure, the nucleotides involved in ligand recognition, specifically C18 and U41, exhibit a closer proximity compared to their arrangement in the bound-form (Figure 4B–D). Distances between specific atoms in C18 and U41 including 4-NH_2 (C18) to O4 (U41), N3 (C18) to N3 (U41), O2 (C18) to O2 (U41), and 2′-OH (C18) to 2′-OH (U41), differ between the two structures. In the THF-bound structure, these distances measure 9.9, 7.5, 5.4 and 7.6 Å, respectively (Figure 4C). However, in the ligand-free form structure, these distances are shorter, measuring 7.8, 6.0, 4.5 and 7.3 Å, respectively (Figure 4D). A comparison of the *B*-factor distribution between the ligand-free and ligand-bound THF-II structures reveals stem P2, positioned above the ligand-sensing cavity in the THF-II riboswitch, displays greater dynamics in the ligand-free structure (Supplementary Figure S8A) than in the ligand-bound structure (Supplementary Figure S8B). These results suggest that THF binding likely contributes to stabilizing the overall structure of the riboswitch, highlighting the role of ligand-induced conformational changes in modulating structural dynamics.

Furthermore, we employed circular dichroism (CD) spectroscopy to systematically investigate the impact of the ligand THF and Mg^{2+} on the structural stabilization of the THF-II riboswitch. As illustrated in Figure 4E, the *env6* THF-II riboswitch displays consistent absorption curves spanning 200–350 nm in the absence of Mg^{2+}, and in the presence of Mg^{2+}, THF and their combination. Subsequent to this, we meticulously monitored the thermal stabilization of the THF-II riboswitch by tracking the signal at the negative peak of 210 nm while systematically elevating the temperature. Notably, in the presence of Mg^{2+}, or with Mg^{2+} and THF combined, the THF-II riboswitch displayed reduced millidegree (mDeg) values (Figure 4F) and high melting temperature (Supplementary Figure S8C). This was observed in comparison to the THF-II riboswitch alone or with THF alone at varying temperatures, emphasizing the pivotal role of Mg^{2+} in reinforcing the overall structural integrity of the THF-II riboswitch.

To further assess the impact of magnesium ions on THF binding capacity of *env6* THF-II riboswitch, an investigation was conducted using *env6* THF-II riboswitch RNA samples prepared with varying Mg^{2+} concentrations (ranging from 0 mM to 5 mM), followed by ITC experiments. The results revealed that concentrations of Mg^{2+} below 0.5 mM were insufficient for THF binding. However, as the Mg^{2+} concentration increased to 5 mM, the binding affinity between *env6* THF-II riboswitch and THF also increased (0.5 mM Mg^{2+}, K_d of 102 μM; 1 mM Mg^{2+}, K_d of 79.9 μM; 5 mM Mg^{2+}, K_d of 12.8 μM) (Supplementary Figure S9 and Supplementary Table S4). Moreover, ITC experiments were conducted to explore the impact of other divalent cations such as Ba^{2+} Ca^{2+} or Mn^{2+}. Intriguingly, as depicted in Supplementary Figure S10 and Supplementary Table S4, Ba^{2+} or Ca^{2+} exhibited a three to four times higher binding affinity for THF compared to the same concentration of Mg^{2+} (5 mM Ba^{2+}, K_d of 3.3 μM; 5 mM Ca^{2+}, K_d of 3.7 μM), while Mn^{2+} exhibited a comparable binding affinity (5 mM Mn^{2+}, K_d of 11.9 μM). These observations underscore the essential role of metal ions in shaping the structure of J1/2 and contributing significantly to the formation of the THF binding pocket (Figure 4G).

Structure-based rational search for the bound compound of THF-II riboswitch

Our structural investigation revealed that the tetrahydropterin part of THF is specifically recognized by C18 and U41, forming a clamp in the binding cavity (Figures 3A–C and 5A). In this configuration, 2-NH_2, N3 and O4 of THF interact with the Watson-Crick edge of C18, while N1, 2-NH_2, and N8 of THF interact with the Watson–Crick edge of U41 (Figures 3C and 5A). Notably, in pterins, the six-atom pyrimidine ring is

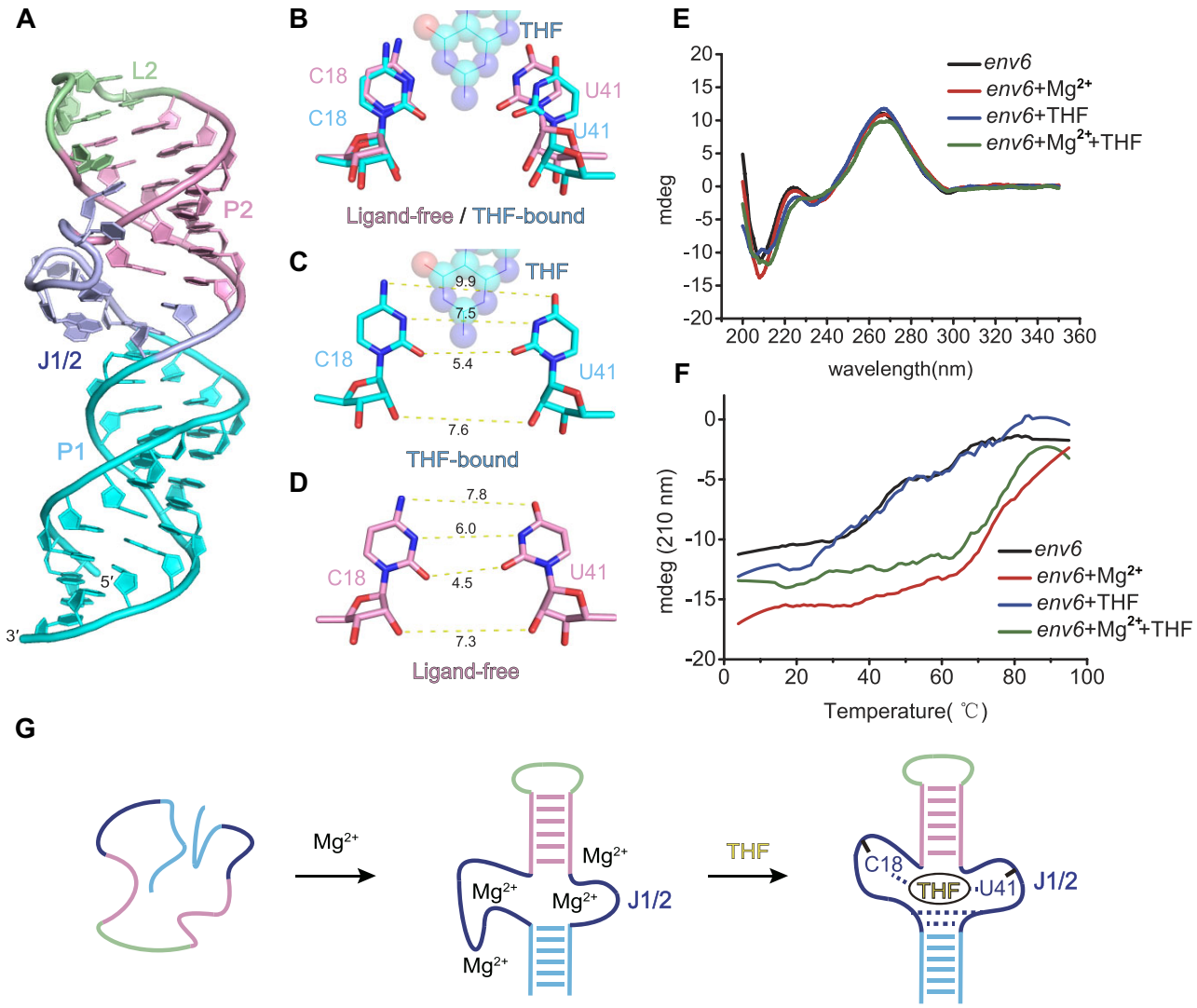

Figure 4. Tertiary structure of free-form THF-II riboswitch. (**A**) Cartoon representation of the tertiary structure of the free-form THF-II riboswitch, same colour code as in the cartoon representation in Figure 1C is used. (**B**) Superposition of THF-bound and free-form THF-II riboswitch nucleotides C18 and U41 (the nucleotides participate in the binding with THF in THF-bound riboswitch). The THF-bound riboswitch nucleotides are shown in cyan, while the free-form riboswitch nucleotides are shown in pink. (**C**) The distances between specific atoms in C18 and U41 in THF-bound riboswitch. (**D**) The distances between specific atoms in C18 and U41 in free-form riboswitch. (**E**) Absorption curves of the *env6* THF-II riboswitch spanning from 200 nm to 350 nm in the absence of Mg^{2+}, and in the presence of Mg^{2+}, THF, and their combination in Circular Dichroism (CD) spectroscopy. (**F**) Recorded mDeg signals of the *env6* THF-II riboswitch at the negative peak of 210 nm with systematically elevating temperature in the absence of Mg^{2+}, and in the presence of Mg^{2+}, THF and their combination. (**G**) Putative folding process of THF-II riboswitches with the help of Mg^{2+}. The metal ions significantly contribute to shaping the structure of J1/2 and the formation of THF binding pocket.

chemically fused with the pyrazine ring, and all interacting atoms in the tetrahydropterin, except N8, are located in the six-atom pyrimidine ring. Positions 5, 6 and 7 of the tetrahydropterin are situated in the pyrazine ring and are not buried in the cavity. Using this information, we conducted a structure-based exploration for compounds capable of interacting with the THF-II riboswitch. Two groups of compounds were investigated: Group 1 involved altering the substituted chemical groups attached to the pyrazine ring, while Group 2 comprised compounds with a five-atom ring, such as imidazole ring, pyrazole ring and triazole ring, replacing the pyrazine ring.

Combining ITC experiments and SPR assays, we successfully identified THF analogs, including DHF, BH_4 and DHN, capable of binding to the THF-II riboswitch (Figure 5A and Supplementary Figures S11-S12). Compared to THF, *env6* THF-II riboswitch displayed similar binding affinity to DHN and BH_4, with K_d values of 12.4 ± 0.2 and 10.6 ± 0.2 μM, respectively (Supplementary Figure S12). However, no binding activity was observed for folinic acid, 6-biopterin, folic acid or 5-methyl THF (Supplementary Figure S13). Furthermore, intriguing findings emerged as guanine and guanine-related analogs, including 8-Me-guanine, 8-NH_2-guanine, and 8-N-guanine, demonstrated a significant binding affinity with the THF-II riboswitch (Figure 5 and Supplementary Figures S14 and S15). ITC experiments were conducted to evaluate the binding of *env6* THF-II riboswitch to guanine, revealing a comparable binding affinity (K_d = 7.2 μM) to that of THF ligand (Figures 1D, 5B and Supplementary Figure S14A).

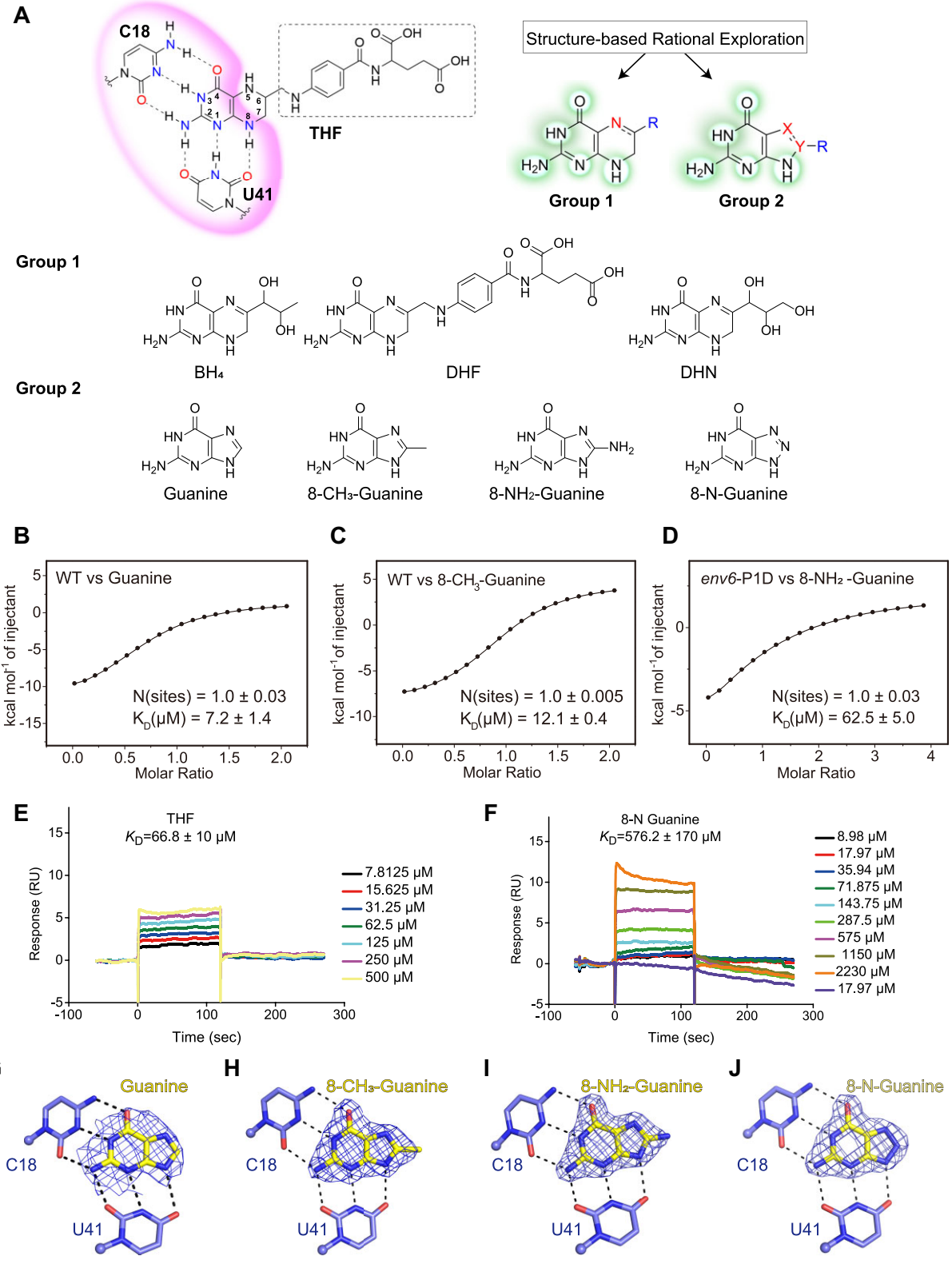

Figure 5. Structure-based rational identification of the compounds binding to THF-II riboswitch. (**A**) Designed compounds capable of interacting with the THF-II riboswitch base on structural information. Group 1 involved altering the substituted chemical groups attached to the pyrazine ring, while Group 2 comprised compounds with a five-atom ring, such as imidazole ring, pyrazole ring, and triazole ring, replacing the pyrazine ring. (B–D) ITC experiment of wild-type THF-II riboswitch binding with guanine (**B**), 8-CH_3-Guanine (**C**), 8-NH_2-Guanine (**D**). (E–F) SPR experiment of wild-type THF-II riboswitch binding with THF (**E**), 8-N-Guanine (**F**). (**G-J**) Binding pocket of THF-II riboswitch recognizing Guanine (**G**), 8-CH_3-Guanine (**H**), 8-NH_2-Guanine (**I**) and 8-N-Guanine (**J**). The purine part of guanine, 8-CH_3-Guanine, 8-NH_2-Guanine, and 8-N-Guanine forms similar hydrogen-bonding interaction with C18 and U41 of THF-II riboswitch. The composite omit maps (contoured at 1.0 σ level) of all the related compounds are shown.

Further ITC experiments indicated that that 8-Me guanine binds to *env6* THF-II RNA with K_d of 11.7 ± 1.4 μM (Figure 5D and Supplementary Figure S14B), while 8-NH2 guanine binds to *env6*-P1D RNA with K_d of 61.1 ± 4.0 μM (Figure 5F and Supplementary Figure S14C). However, 8-azaguanine displayed a lower binding affinity with a K_d of approximately 576 μM in SPR assay, potentially attributed to tautomeric interconversion within 8-azaguanine (Figure 5F and Supplementary Figure S15A).

We have successfully performed co-crystallization and structural determination of *env6* THF-II riboswitches in complexes with BH_4, DHF or DHN. Alignments of the overall 3D-folds of the riboswitch bound to THF, BH_4, DHF and DHN reveals significant identity. THF, BH_4, DHF and DHN exhibit same recognition modes within the binding pocket (Figure 3C and Supplementary Figure S15B–D), where the tetrahydropterin part of them are almost completely encapsulated by THF-II riboswitch, leaving other substructures of ligands outside of the binding pocket without restraint (Supplementary Figure S15B–D). The replacement of *para*-amino-benzoic acid and the glutamic acid part by a propylene glycol group (as in BH_4) or a propanetriol group (as in DHN) retains the tetrahydropterin part, ensuring effective recognition by the THF-II riboswitch. However, in both folic acid and 6-biopterin, N8 of the tetrahydropterin part is present in oxidized form, impairing the hydrogen bond interaction between the riboswitch and N8 in reduced form (Supplementary Figure S13). Similarly, in both folinic acid and 5-methyl THF, N5 of the tetrahydropterin part is modified by formyl and methyl group, larger than a proton, preventing binding with THF-II riboswitch, as confirmed by ITC experiments (Supplementary Figure S13). We attribute this distinction from THF by steric hindrance.

Co-crystallization of *env6* THF-II riboswitch RNA with guanine has produced high-quality diffracting crystals. The guanine-bound riboswitch structure was determined by molecular replacement (MR) method with THF-bound THF-II riboswitch complex as the initial structural model (Figure 5G). As anticipated, the Watson–Crick edge (O6, N1, 2-NH_2) of guanine forms three hydrogen bonds with Watson–Crick edge of C18, while the sugar edge (N9, N3, 2-NH_2) of guanine forms three additional hydrogen bonds with the Watson–Crick edge of U41(Figure 5G). These results indicate that the binding cavity of THF-II riboswitch interacts with guanine using the same recognition pattern as THF, but with a slight elasticity to accommodate additional potential compounds besides the tetrahydropterin part. Furthermore, we co-crystallized 8-methyl guanine (8-CH_3 guanine), 8-aminoguanine (8-NH_2 guanine) and 8-N guanine with *env6* THF-II riboswitch RNA and successfully obtained the three-dimensional structures by molecular replacement (MR) method respectively. Similar to the guanine-bound structure, both 8-Me guanine, 8-NH_2 guanine and 8-N guanine bind with THF-II riboswitch through Watson-Crick and sugar edges, employing the same binding pattern with guanine. The Watson–Crick edge (O6, N1, 2-NH_2) forms three hydrogen bonds with Watson–Crick edge of C18, and the sugar edge (N9, N3, 2-NH_2) forms three hydrogen bonds with the Watson–Crick edge of U41 (Figure 5H–J).

Concluding remarks

We determined the structures of THF-II riboswitches in both the free-form and bound-form (Figures 1 and 4), revealing overall high similarity with minor variation in the local nucleotide arrangement surrounding the ligand-binding site (Figure 4 and Supplementary Figure S7). Subsequent CD spectroscopy indicates that Mg^{2+} significantly contributes to stabilizing THF-II riboswitches, resulting in an elevated melting temperature (Supplementary Figure S8C). ITC experiments show that THF-II riboswitches exhibit minimal binding affinity to THF in the absence of Mg^{2+} or at low concentrations (Supplementary Figure S9). This suggests that Mg^{2+} facilitates the folding of THF-II riboswitches in the absence of ligand, allowing pre-folded RNA molecules to interact with ligands when ligands are present (Figure 4G). The results align with the intrinsic property of RNA molecules, where negatively charged RNA molecules often rely on cations for folding and functioning, and enhance our understanding of the ligand recognition process and mechanisms of RNA molecules.

In our structure-based search of the small molecules that interact with THF-II riboswitches. We not only confirmed the binding of THF derivatives, such as BH_4, DHF and DHN, but also identified the binding capacity of guanine and its derivatives, including 8-Me-guanine, 8-NH_2-guanine, and 8-N-guanine, to THF-II riboswitch. These findings highlight the versatility of the THF-II riboswitch in recognizing ligands, showcasing its ability to accommodate structurally related molecules. As purine analogs, Guanine and its derivatives have been extensively investigated for their potential biological activities (28). Our structure-based discovery involving 8-substituted guanine derivatives, including 8-Me-guanine, 8-NH_2-guanine, and 8-N-guanine and the subsequent experimental validation of their interaction with THF-II riboswitches, not only expands the chemical space of compounds targeting THF-II riboswitches, but also highlight the significance of structure determination in developing small molecules that target RNA molecules. The distribution of THF-II riboswitches in certain pathogens, such as *Brucella* and *Ochrobactrum* (18), amplifies the significance of our findings. This discovery holds the potential to introduce innovative strategies in drug development, particularly in crafting compounds designed to combat pathogens exploiting THF-II riboswitches. Furthermore, it opens promising avenues for the advancement of therapeutic development related to riboswitches.

Data availability

Atomic coordinates and structure factors for the reported crystal structures of *env6* THF-II riboswitch in complex with THF and other analogs have been deposited with the Protein Data bank (www.rcsb.org) under accession numbers 8XZE (*env6*-THF $Ir(NH_3)_6^{3+}$ soaking structure), 8XZK (*env6* ligand-free structure), 8XZL (*env6*-DHF structure), 8XZM (*env6*-DHN structure), 8XZN(*env6*-BH_4 structure), 8XZO (*env6*-Guanine structure), 8XZP (*env6*-8-CH_3-Guanine structure), 8XZQ (*env6*-8-N-Guanine structure), 8XZR (*env6*-8-NH_2-Guanine structure), and 8XZW (*env6*-THF structure) respectively. All study data are included in the article and or *Supplementary Materials*.

Supplementary data

Supplementary Data are available at NAR Online.

Acknowledgements

We thank the staff members of the Large-scale Protein Preparation System, BL-17B, BL-17U1, BL18U1, and BL-19U1 beamlines at the National Facility for Protein Science in Shanghai (NFPS), Zhangjiang Lab, China for providing technical support and assistance in data collection and analysis. We thank the staff of the BL-17U1 beamline at the National Center for Protein Sciences Shanghai (NCPSS) at SSRF for their assistance in X-ray data collection. We thank the technical assistance from the core facility of the Life Sciences Institute (LSI), Zhejiang University.

Funding

National Natural Science Foundation of China [32325029, 91940302, 91640104 to A.R.]; National Key Research and Development Project of China [2023YFC2604300, 2021YFC2300300 to A.R.]. Funding for open access charge: Research grant.

Conflict of interest statement

None declared.

References

1. Winkler,W.C., Cohen-Chalamish,S. and Breaker,R.R. (2002) An mRNA structure that controls gene expression by binding FMN. *Proc. Nat. Acad. Sci. U.S.A.*, **99**, 15908–15913.
2. Winkler,W., Nahvi,A. and Breaker,R.R. (2002) Thiamine derivatives bind messenger RNAs directly to regulate bacterial gene expression. *Nature*, **419**, 952–956.
3. Nahvi,A., Sudarsan,N., Ebert,M.S., Zou,X., Brown,K.L. and Breaker,R.R. (2002) Genetic control by a metabolite binding mRNA. *Chem. Biol.*, **9**, 1043.
4. Mironov,A.S., Gusarov,I., Rafikov,R., Lopez,L.E., Shatalin,K., Kreneva,R.A., Perumov,D.A. and Nudler,E. (2002) Sensing small molecules by nascent RNA: a mechanism to control transcription in bacteria. *Cell*, **111**, 747–756.
5. Jones,C.P. and Ferre-D'Amare,A.R. (2017) Long-range interactions in riboswitch control of gene expression. *Annu. Rev. Biophys.*, **46**, 455–481.
6. Serganov,A. and Nudler,E. (2013) A decade of riboswitches. *Cell*, **152**, 17–24.
7. Breaker,R.R. (2012) Riboswitches and the RNA world. *Cold Spring Harb. Perspect. Biol.*, **4**, a003566.
8. Garst,A.D., Edwards,A.L. and Batey,R.T. (2011) Riboswitches: structures and mechanisms. *Cold Spring Harb. Perspect. Biol.*, **3**, a003533.
9. Breaker,R.R. (2022) The biochemical landscape of riboswitch ligands. *Biochemistry*, **61**, 137–149.
10. McCown,P.J., Corbino,K.A., Stav,S., Sherlock,M.E. and Breaker,R.R. (2017) Riboswitch diversity and distribution. *RNA*, **23**, 995–1011.
11. Cochrane,J.C. and Strobel,S.A. (2008) Riboswitch effectors as protein enzyme cofactors. *RNA*, **14**, 993–1002.
12. Serganov,A. and Patel,D.J. (2012) Metabolite recognition principles and molecular mechanisms underlying riboswitch function. *Annu. Rev. Biophys.*, **41**, 343–370.
13. Bermingham,A. and Derrick,J.P. (2002) The folic acid biosynthesis pathway in bacteria: evaluation of potential for antibacterial drug discovery. *Bioessays*, **24**, 637–648.
14. Suh,J.R., Herbig,A.K. and Stover,P.J. (2001) New perspectives on folate catabolism. *Annu. Rev. Nutr.*, **21**, 255–282.
15. Ames,T.D., Rodionov,D.A., Weinberg,Z. and Breaker,R.R. (2010) A eubacterial riboswitch class that senses the coenzyme tetrahydrofolate. *Chem. Biol.*, **17**, 681–685.
16. Trausch,J.J., Ceres,P., Reyes,F.E. and Batey,R.T. (2011) The structure of a tetrahydrofolate-sensing riboswitch reveals two ligand binding sites in a single aptamer. *Structure*, **19**, 1413–1423.
17. Huang,L., Ishibe-Murakami,S., Patel,D.J. and Serganov,A. (2011) Long-range pseudoknot interactions dictate the regulatory response in the tetrahydrofolate riboswitch. *Proc. Nat. Acad. Sci. U.S.A.*, **108**, 14801–14806.
18. Chen,X., Mirihana Arachchilage,G. and Breaker,R.R. (2019) Biochemical validation of a second class of tetrahydrofolate riboswitches in bacteria. *RNA*, **25**, 1091–1097.
19. Sun,A., Huang,K., Zheng,L. and Ren,A. (2019) In: Hargrove,A.E. (ed). *RNA Recognition*. Vol. **623**, pp. 229–248.
20. Riccitelli,N. and Luptak,A. (2013) HDV family of self-cleaving ribozymes. *Prog. Mol. Biol. Transl. Sci.*, **120**, 123–171.
21. Schneider,T.P.T.R. (2004) HKL2MAP: a graphical user interface for phasing with SHELX programs. *J. Appl. Cryst.*, **37**, 843–844.
22. Murshudov,G.N., Vagin,A.A. and Dodson,E.J. (1997) Refinement of macromolecular structures by the maximum-likelihood method. *Acta Crystallogr. Sect. D Biol. Crystallogr.*, **53**, 240–255.
23. Emsley,P. and Cowtan,K. (2004) Coot: model-building tools for molecular graphics. *Acta Crystallogr. Sect. D Biol. Crystallogr.*, **60**, 2126–2132.
24. Adams,P.D., Afonine,P.V., Bunkoczi,G., Chen,V.B., Davis,I.W., Echols,N., Headd,J.J., Hung,L.W., Kapral,G.J., Grosse-Kunstleve,R.W., *et al.* (2010) PHENIX: a comprehensive Python-based system for macromolecular structure solution. *Acta. Crystallogr. D Biol. Crystallogr.*, **66**, 213–221.
25. Sun,Z., Liu,Q., Qu,G., Feng,Y. and Reetz,M.T. (2019) Utility of B-factors in protein science: interpreting rigidity, flexibility, and internal motion and engineering thermostability. *Chem. Rev.*, **119**, 1626–1665.
26. Zhang,M., Liu,G., Zhang,Y., Chen,T., Feng,S., Cai,R. and Lu,C. (2022) The second class of tetrahydrofolate (THF-II) riboswitches recognizes the tetrahydrofolic acid ligand via local conformation changes. *Int. J. Mol. Sci.*, **23**, 5903–5914.
27. Xu,L., Xiao,Y., Zhang,J. and Fang,X. (2023) Structural insights into translation regulation by the THF-II riboswitch. *Nucleic Acids Res.*, **51**, 952–965.
28. Jackson,E.K., Menshikova,E.V., Ritov,V.B., Mi,Z. and Birder,L.A. (2022) 8-Aminoinosine and 8-aminohypoxanthine inhibit purine nucleoside phosphorylase and exert diuretic and natriuretic activity. *J. Pharmacol. Exp. Ther.*, **382**, 135–148.

Received: March 14, 2024. **Revised:** April 23, 2024. **Editorial Decision:** April 24, 2024. **Accepted:** April 26, 2024